UNIVERSITY OF AMSTERDAM

UvA-DARE (Digital Academic Repository)

Chlorine and potassium enrichment in the Cassiopeia A supernova remnant

XRISM collaboration

DOI
10.1038/s41550-025-02714-4

Publication date
2026

Document Version
Final published version

Published in
Nature Astronomy

License
CC BY-NC-ND

Link to publication

Citation for published version (APA):
XRISM collaboration (2026). Chlorine and potassium enrichment in the Cassiopeia A supernova remnant. *Nature Astronomy*, *10*, 144–153. https://doi.org/10.1038/s41550-025-02714-4

General rights
It is not permitted to download or to forward/distribute the text or part of it without the consent of the author(s) and/or copyright holder(s), other than for strictly personal, individual use, unless the work is under an open content license (like Creative Commons).

Disclaimer/Complaints regulations
If you believe that digital publication of certain material infringes any of your rights or (privacy) interests, please let the Library know, stating your reasons. In case of a legitimate complaint, the Library will make the material inaccessible and/or remove it from the website. Please Ask the Library: https://uba.uva.nl/en/contact, or a letter to: Library of the University of Amsterdam, Secretariat, P.O. Box 19185, 1000 GD Amsterdam, The Netherlands. You will be contacted as soon as possible.

UvA-DARE is a service provided by the library of the University of Amsterdam (https://dare.uva.nl)

Download date:08 Sept 2026

nature astronomy

Article

https://doi.org/10.1038/s41550-025-02714-4

Chlorine and potassium enrichment in the Cassiopeia A supernova remnant

Received: 31 July 2025

Accepted: 14 October 2025

Published online: 4 December 2025

Check for updates

XRISM collaboration*

The elements in the Universe are synthesized primarily in stars and supernovae, where nuclear fusion favours the production of even-*Z* elements. In contrast, odd-*Z* elements are less abundant and their yields are highly dependent on detailed stellar physics, making theoretical predictions of their cosmic abundance uncertain. In particular, the origin of odd-*Z* elements such as phosphorus (P), chlorine (Cl) and potassium (K), which are important for planet formation and life, is poorly understood. While the abundances of these elements in Milky Way stars are close to solar values, supernova explosion models systematically underestimate their production by up to an order of magnitude, indicating that key mechanisms for odd-*Z* nucleosynthesis are currently missing from theoretical models. Here we report the observation of P, Cl and K in the Cassiopeia A supernova remnant using high-resolution X-ray spectroscopy with X-Ray Imaging and Spectroscopy Mission data, with the detection of K at above the 6σ level being the most significant finding. Supernova explosion models of normal massive stars cannot explain the element abundance pattern, especially the high abundances of Cl and K, while models that include stellar rotation, binary interactions or shell mergers agree closely with the observations. Our observations suggest that such stellar activity plays an important role in supplying these elements to the Universe.

Observing the chemical composition of supernovae (SNe) and supernova remnants (SNRs) provides direct evidence of how elements are synthesized and distributed in the Universe. The elemental abundance patterns of these objects or stars reflect the physical processes occurring in stellar interiors and explosions[1–3], offering crucial insights into the origin and evolution of elements. While even-*Z* elements (that is, α-elements) have been extensively studied in SNe and SNRs, observations of odd-*Z* elements, such as phosphorus (P), chlorine (Cl) and potassium (K), remain scarce, and their theoretical treatment is incomplete[4,5]. Notably, galactic chemical evolution models struggle to explain the observed abundances of these elements[6–9], and discrepancies with theoretical predictions have also been reported in observations of some metal-poor stars[10]. These inconsistencies highlight a fundamental gap in our understanding of nucleosynthesis processes. Currently, stellar processes such as rotation, binary interactions and shell mergers (the merging of adjacent nuclear-burning shells into a single convective shell) have been proposed as plausible mechanisms to resolve this issue[9,11,12]. Here, the nucleosynthesis pathways for odd-*Z* element production, which include γ-reactions and neutron/proton capture, are complex[11], and it is necessary to directly discuss the synthesis yields of these elements on the basis of observations. However, because emission lines from odd-*Z* elements are faint, it has been difficult to observe them in SNe/SNRs with existing detectors (particularly in X-rays), and their origin therefore remains unresolved.

Recent near-infrared spectroscopic studies of Cassiopeia A, the youngest known core-collapse SNR in our Galaxy, have reported the detection of emission from P (refs. 4,13). In particular, its [P/Fe] ratio is up to 100 times higher than the average in the Milky Way[4], prompting

*A list of authors and their affiliations appears at the end of the paper. ✉e-mail: toshiki@meiji.ac.jp; uchida@cr.scphys.kyoto-u.ac.jp; matsunaga.kai.i47@kyoto-u.jp

https://doi.org/10.1038/s41550-025-02714-4

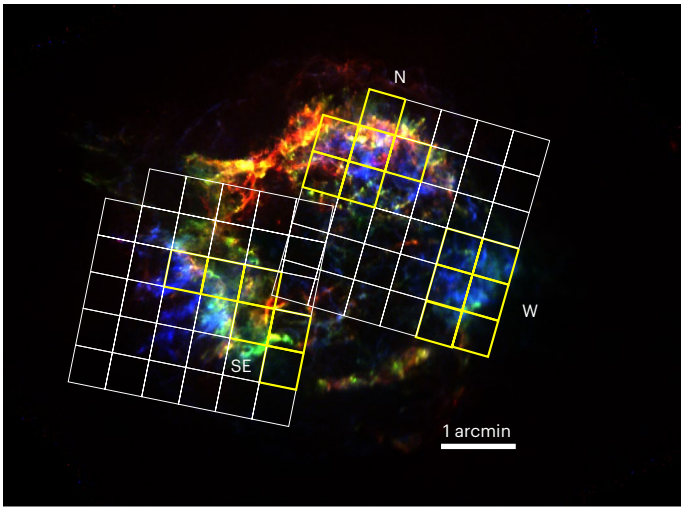

Fig. 1 | Three-colour image of the core-collapse SNR Cas A. Red, green and blue represent Chandra X-ray images of O- (0.6–0.85 keV), Si- (1.76–1.94 keV) and Fe-enhanced (6.54–6.92 keV) regions, respectively. The white grids indicate the fields of view of our two-pointing observations with XRISM/Resolve, which has a 6 × 6 pixel array: a pixel at a corner is only used for calibration. Pixels we selected for our spectral analysis are highlighted in yellow. In the south-east (SE) and north (N) regions, we examined the spectrum of each pixel and selected those exhibiting large equivalent widths of K emission; the spatial distribution of these pixels closely matches that of the O and Si emission lines. In contrast, the west (W) region exhibits weak O line intensity, and the K emission line in its spectrum is faint (Fig. 2).

a discussion on the nucleosynthesis processes during the SN explosion. However, the observed [P/Fe] ratios were scattered by about two orders of magnitude in the remnant because the two elements are synthesized at different locations and unevenly mixed in a SN, preventing a clear understanding of their origin. In addition, since most of the SN ejecta have already been heated by the reverse shock ($\lesssim$20% of ejecta are unshocked)[14], X-ray emission from the shocked ejecta most accurately reflects the true elemental composition in the remnant. To fully understand the origin of odd-Z elements, it is thus crucial to systematically measure the abundances of several odd-Z elements, including Cl and K, together with neighbouring even-Z elements (for example, Si, S, Ar and Ca) produced at the same site using X-ray spectroscopy. Therefore, high-resolution non-dispersive X-ray spectroscopy, which has the potential to observe all these elements, is a unique tool to probe the nucleosynthesis of odd-Z elements produced in SNe.

The X-Ray Imaging and Spectroscopy Mission (XRISM)[15], successfully launched on 7 September 2023, is equipped with the Resolve microcalorimeter, capable of non-dispersive high-resolution spectroscopy ($\Delta E < 7$ eV, where ΔE denotes the energy resolution) in the X-ray band (1.7–10 keV), where primary emission lines from ionized elements P, Cl and K are emitted. We conducted observations of Cas A with XRISM twice in mid-December 2023 (Fig. 1, Table 1 and 'Observation and data reduction' section in the Methods). These two pointings cover the majority of the remnant's SN ejecta, with the exception of the north-east-extending jet-like structure, enabling a comprehensive investigation of odd-Z elements in this remnant. Notably, large clumps of ejecta are concentrated in the south-east, north and west regions, reflecting the explosion's asymmetry[16]. As shown in the Chandra elemental maps (Fig. 1), the south-east and north blobs contain O-rich ejecta (most probably the product of hydrostatic nuclear fusion in the progenitor star's deep interior) along with Fe- and Si-rich ejecta (the products of the explosive nucleosynthesis). In contrast, the west region is dominated by Fe and Si. We employ spatially resolved spectroscopy with XRISM/Resolve to examine and compare the elemental abundances across these distinct regions.

Table 1 | Observation log of Cas A with XRISM

Target name	Sequential no.	Start date of observation	Exposure time (ks)
Cas A SE	000129000	11 December 2023, 05:49:47	181.3
Cas A NW	000130000	14 December 2023, 14:38:50	166.6

'Sequential no.' is the identifier assigned to each observation made by XRISM. 'Exposure time' is the net duration of the observations after data screening. The observation start time is defined in Coordinated Universal Time (UTC).

Figure 2 shows the X-ray spectra of the north (N), south-eastern (SE) and western (W) regions of Cas A. In the SE and N regions, Resolve clearly detected the emission from highly ionized He-like ions of Cl and K (at $\gtrsim 5\sigma$ and $>6\sigma$ confidence levels, respectively). In contrast, the W region shows no clear line structures and only marginal Cl- and K-line detection significances ($<2\sigma$). Marginal evidence of P is also detected in the SE and W regions ($\gtrsim 4\sigma$ confidence level; Table 2 and Extended Data Table 1). These results reveal a spatially inhomogeneous distribution of odd-Z elements in Cas A, with their emission confined to the O-rich regions in the north and south-east but absent in the western region. These detections are unaffected by background emission, spatial–spectral mixing from the telescope's point spread function, fitting range choices or other factors (Methods and Extended Data Table 1). The abundance ratios relative to hydrogen are approximately 3–5 solar values, confirming that these elements originate from the SN ejecta rather than the interstellar medium. Dielectronic recombination and inner-shell excitation lines from other elements lie close to the P and Cl line features, with the former being almost completely overlapped and the latter located immediately adjacent, making accurate abundance estimates dependent on careful plasma modelling. In the K band, there are no prominent contaminating lines, allowing for a clean separation of the emission feature. The N region shows complex velocity structures in intermediate-mass elements (see fig. 4 in ref. 17), making abundance measurements there less reliable (see the Methods for detail). We therefore adopt the K/Ar and Cl/S ratios from the SE region as representative values, with the K/Ar ratio being the most reliable owing to its clear detection and minimal contamination, and the Cl/S ratio also being considered reasonably robust. The Cl/S ratio is estimated to be $(\mathrm{Cl/S})/(\mathrm{Cl/S})_\odot = 1.0 \pm 0.1$ and the K/Ar ratio $(\mathrm{K/Ar})/(\mathrm{K/Ar})_\odot = 1.3 \pm 0.2$, on the basis of proto-solar values from ref. 18. Here, we use the abundance ratios relative to neighbouring even-Z elements to examine the characteristics of the synthesis processes in the subsequent discussion. Across a variety of fitting conditions, the derived abundance ratios remain consistent within a range of ~10–40%, which probably reflects the level of systematic uncertainty in our measurements and does not affect our conclusions (see 'Spectral analysis' section in the Methods and Extended Data Table 1).

The observed ratios close to the solar value suggest abundant production of Cl and K in the remnant, in contrast to the scarcity in the theoretical models[8]. Figure 3 shows the elemental mass ratios from Si to Ca (relative to Ar) obtained from our observation of the SE region. It is noteworthy that the observed K and Cl abundances in Cas A, whose initial progenitor mass is estimated to be close to 15 $M_\odot$ (ref. 19), are significantly higher than those in SN models within the initial mass range of 13–25$M_\odot$ from ref. 20 (hereafter NKT13), whereas the observed abundances of the even-Z elements roughly follow the trend of the models (see Extended Data Fig. 1 for a more detailed comparison). This implies that some mechanisms not included in the models enhanced the abundance of the odd-Z elements in Cas A. The fact that these Cl and K emission are spatially associated with the O-rich ejecta suggests that their production was amplified during the stellar evolution stage rather than being solely the result of explosive nucleosynthesis. Regarding the P abundance, both observational uncertainties and large variations among theoretical models make quantitative discussion difficult

https://doi.org/10.1038/s41550-025-02714-4

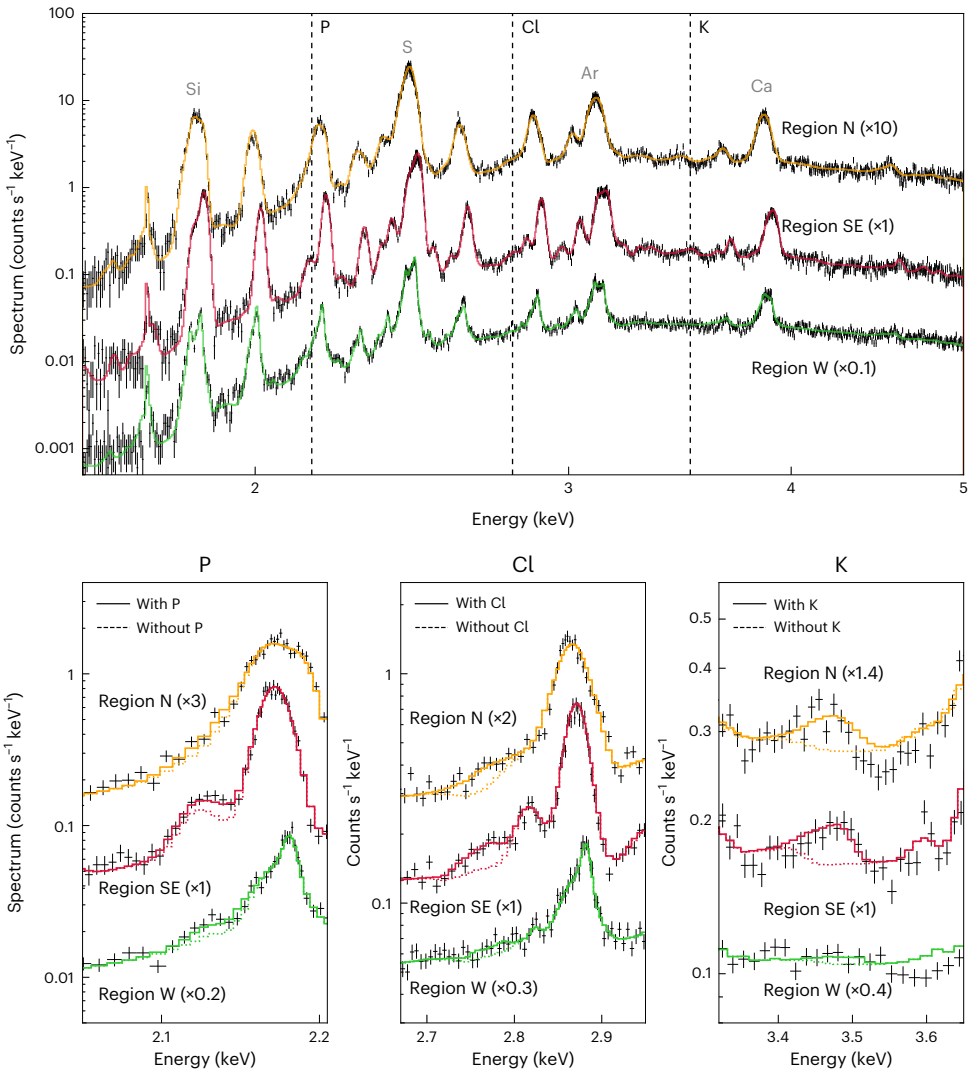

Fig. 2 | Resolve X-ray spectra of Cas A. The best-fit models are overplotted as a solid line, with colours representing the spectral regions in Fig. 1 (orange, N region; red, SE region; green, W region). In the top panel, the labels indicate the positions of the He α emission lines for each element. The vertical broken lines correspond to the centroid energies of the resonance lines of P (~2.152 keV), Cl (~2.790 keV) and K (~3.511 keV) in the rest frame. The bottom three panels show the zoom-in spectra around He α P (left), Cl (middle) and K (right) line with the best fit models with or without the K emission line. In the spectra of the P band, models without P emission show residuals near 2.13 keV, particularly in the SE and W regions, indicating the signature of P emission in the spectra, while no significant residual is seen in the N region. In the Cl and K bands, models lacking the corresponding lines show residuals in the N and SE regions but not in the W region. The intermediate-mass elements, particularly in the N region, exhibit complex velocity structures (see fig. 4 in ref. 17), which introduces modelling uncertainties. For clarity, the spectrum of the SE region is shifted slightly along the energy axis in the zoomed-in panels. The horizontal and vertical error bars indicate the selected energy range for each bin and the 1σ statistical uncertainty, respectively.

at this stage (Extended Data Table 1), even though the measured value falls within the range of theoretical predictions in Fig. 3.

Some stellar activities have been proposed to explain the enhanced production of odd-Z elements in massive stars, most notably stellar rotation[9], binary interactions[12] and the shell merger phenomenon[11]. To investigate these effects, we compare the observed Cl/S and K/Ar ratios with predictions from several core-collapse SN nucleosynthesis models in Fig. 4: non-rotating single-star models from NKT13, rotating models from ref. 21, shell merger candidates from ref. 22 and binary-star models from ref. 12 (see Extended Data Fig. 2 for a more detailed comparison). The models with the stellar effects tend to have higher Cl/S and K/Ar ratios than those of the NKT13 models, implying that these processes are required to explain our observations. In particular, some of the shell merger and binary models predict ratios exceeding those measured in Cas A, indicating an efficient odd-Z production mechanism in these scenarios. However, we note that these models involve large uncertainties. In the case of shell merger models, the predicted yields are highly sensitive to the multi-dimensional mixing in the burning layer[11]. Furthermore, Farmer et al.[12] point out that, in their binary models, the convective structure near the nucleosynthesis region may introduce substantial uncertainties in the production of these elements. Since our work presents the observational constraint on Cl and K abundances in a core-collapse SN, further theoretical development will be crucial to elucidating their production mechanisms. Detailed comparison and extended discussion of our model analysis are provided in 'Model dependence on odd-Z yields' section in the Methods. These interpretations are constrained by current model uncertainties, highlighting the need for future efforts to fully integrate observational and theoretical constraints across diverse progenitor scenarios, as well as for population studies combined with theoretical modelling to determine the prevalence of candidate mechanisms among massive star progenitors.

The observational characteristics of the Cas A remnant are generally more consistent with a progenitor that would support these stellar

Table 2 | Best-fit parameters of spectral fits

Region	SE region		W region	N region
Atomic database	AtomDB	SPEX	AtomDB	AtomDB
$(P/Si)/(P/Si)_\odot$	0.9±0.2	0.9±0.2	1.7±0.4	0.8±0.2
$(Cl/S)/(Cl/S)_\odot$	1.0±0.1	$0.7^{+0.2}_{-0.1}$	0.9±0.3	0.9±0.1
$(K/Ar)/(K/Ar)_\odot$	1.3±0.2	1.2±0.2	0.5±0.3	1.1±0.2
$(Mg/H)/(Mg/H)_\odot$	1.9±0.2	2.5±0.4	1.4±0.3	3.1±0.3
$(Al/H)/(Al/H)_\odot$	2.1±0.5	$2.1^{+0.8}_{-0.7}$	<0.7	<0.5
$(Si/H)/(Si/H)_\odot$	3.67±0.04	4.19±0.09	1.59±0.04	$3.79^{+0.05}_{-0.09}$
$(P/H)/(P/H)_\odot$	$3.5^{+0.7}_{-0.6}$ (5.5σ)	3.6±0.8 (4.7σ)	$2.7^{+0.6}_{-0.7}$	$3.1^{+0.7}_{-0.8}$
$(S/H)/(S/H)_\odot$	$4.04^{+0.04}_{-0.03}$	4.23±0.09	$1.85^{+0.03}_{-0.04}$	$4.68^{+0.09}_{-0.11}$
$(Cl/H)/(Cl/H)_\odot$	$4.2^{+0.5}_{-0.6}$ (7.7σ)	$3.1^{+0.7}_{-0.6}$ (4.8σ)	$1.6^{+0.6}_{-0.5}$	$4.3^{+0.7}_{-0.6}$
$(Ar/H)/(Ar/H)_\odot$	3.55±0.06	$3.74^{+0.09}_{-0.08}$	$1.83^{+0.05}_{-0.06}$	$4.22^{+0.08}_{-0.07}$
$(K/H)/(K/H)_\odot$	$4.5^{+0.7}_{-0.6}$ (7.0σ)	$4.6^{+0.8}_{-0.7}$ (6.3σ)	$0.9^{+0.6}_{-0.5}$	$4.8^{+0.8}_{-0.7}$
$(Ca/H)/(Ca/H)_\odot$	3.60±0.07	3.69±0.09	$2.26^{+0.07}_{-0.03}$	5.14±0.09
$kT_{e,1}$ (keV)	0.92±0.02	0.70±0.03	1.16±0.03	$0.61^{+0.01}_{-0.04}$
$kT_{e,2}$ (keV)	2.13±0.02	2.18±0.06	$1.78^{+0.02}_{-0.03}$	$1.98^{+0.03}_{-0.01}$
$n_e t_1$ (10^{10} cm^{-3} s)	$3.10^{+0.10}_{-0.09}$	4.9±0.4	28^{+5}_{-6}	$4.0^{+0.7}_{-0.3}$
$n_e t_2$ (10^{11} cm^{-3} s)	$1.86^{+0.05}_{-0.03}$	1.90±0.07	$2.2^{+0.1}_{-0.2}$	1.64±0.04
Redshift z_1 (10^{-3})	−3.8±0.1	−3.9±0.2	$0.53^{+0.08}_{-0.06}$	−0.34±0.2
Redshift z_2 (10^{-3})	−4.11± 0.04	−4.11±0.06	4.3±0.1	$6.20^{+0.09}_{-0.04}$
R.m.s. V_1 (km s^{-1})	1,380±30	1,370±40	480^{+30}_{-20}	$1{,}030^{+40}_{-30}$
R.m.s. V_2 (km s^{-1})	1,340±10	1,340±10	1,830±30	1,920±20
C value/d.o.f.	7,438.28/6777	1,613.18/1248	7,053.81/6,780	7,208.06/6,777

The elemental ratios show elemental abundance ratios relative to the solar values. k is the Boltzmann constant, T_e is the electron temperature, $n_e t$ is the ionization timescale and V represents the thermal velocity of the ions. The subscripts "1" and "2" denote the low-temperature and high-temperature plasma components, respectively. C is the fit statistic defined in the Cash statistics. R.m.s. and d.o.f. stand for the root-mean-square and the degrees of freedom, respectively. The error represents a 1σ statistical uncertainty.

processes than the standard stellar nucleosynthesis. As the remnant of a type IIb SN, Cas A probably lost most of its hydrogen envelope through binary interaction[23]. Its extremely low neon (Ne) abundance (Ne/O ≈ 0.1 solar)[24–26], in contrast to the typical Ne/O ≈ 1 solar observed in other SNRs[27,28], further suggests unusual stellar processes that deplete Ne. Stellar phenomena such as rotation and shell mergers have been proposed to account for this Ne scarcity in the O-rich layers of the progenitor star[26,29,30], implying a possible connection between Ne depletion and the enrichment of odd-Z elements during the stellar evolution of Cas A. In addition, our observation reveals a positive correlation between O emission intensity and odd-Z element abundances, further supporting a stellar nucleosynthetic origin. Although the odd-Z enhancement mechanism remains debated[11,12,21], this observational link between stellar activity and odd-Z element synthesis provides a unique benchmark. Interestingly, both the O-rich ejecta and odd-Z elements display a biased distribution from south-east to north in the remnant, which may suggest the impact of asymmetric convection in the stellar interior on SN dynamics[31,32]. Future observations of the odd-Z elements in Cas A and other remnants, using XRISM or upcoming X-ray observatories, will provide deeper insights into pre-SN activities and may hold the key to unveiling the chemical history of our Galaxy.

Methods

Observation and data reduction

We carried out a two-pointing observation of Cassiopeia A (Cas A) during the XRISM commissioning phase as summarized in Table 1 refs. 17,33,34. The Resolve fields of view are shown in Fig. 1. Since the Resolve aperture door ('gate valve') has not opened yet, a 250-μm-thickness beryllium filter attenuates X-ray photons in the soft X-ray band, reducing the effective area. The available energy bandpass in our analysis is above approximately 1.6 keV. The data reduction was done by using calibration data archived in the High Energy Astrophysics Science Archive Research Center (HEASARC) calibration database (CALDB). Cleaned event data were obtained using the latest release version of the HEASARC software (version 6.34) with the standard screening during post-pipeline processing. We only used the highest energy resolution ('Hp') primary events for the spectral analysis. The redistribution matrix file was generated with the extra large size option using 'rslmkrmf'. The ancillary response file was created using 'xaarfgen', assuming the surface brightness of Cas A as derived from a Chandra X-ray image in the 2.0–8.0-keV band.

Energy scale reconstruction

The gain of the XRISM/Resolve calorimeter detectors is intrinsically unstable since the thermal detectors respond to their thermal environment. The XRISM observatory includes multiple on-board calibration sources to track the time-dependent gain of the Resolve instrument and reconstruct the energy scale for each observation. The Cas A observations were performed early in the performance and verification phase of the mission while the gain reconstruction strategy was still being formalized. Currently, gain fiducials are acquired sparsely, approximately twice per day on average, to sample the slow drift of the detector gain due to changes in spacecraft attitude and the thermal recovery from recycling the sub-kelvin adiabatic demagnetization

https://doi.org/10.1038/s41550-025-02714-4

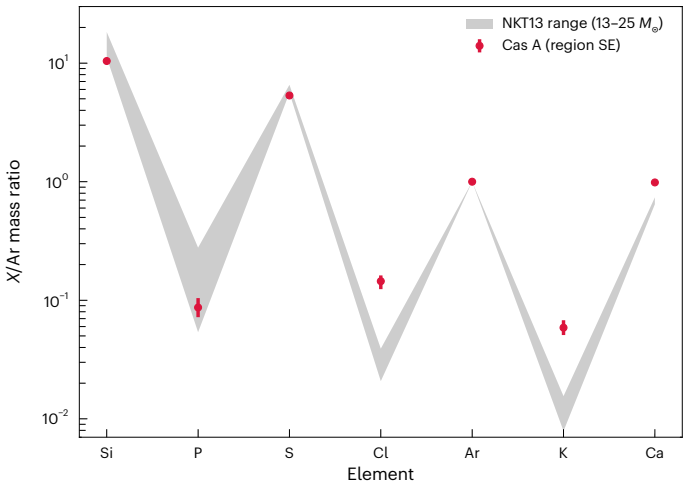

Fig. 3 | Elemental mass ratios in Cas A compared with those in SN nucleosynthesis models. Red circles with error bars represent the mass ratios relative to Ar derived from different regions shown in Fig. 1. The error bar shows a 1σ statistical uncertainty. The grey region indicates the range predicted by core-collapse SN nucleosynthesis models in ref. 20, assuming single-star, non-rotating progenitors with solar metallicity and initial masses in the range of 13–25$M_\odot$. To facilitate comparison between the observed values and the model values, only the model values are connected and that range is shaded. See Extended Data Fig. 2 for a more comprehensive comparison across a wider range of model parameters.

refrigerator. However, the Cas A observations were performed with much more frequent sampling of the gain: once every other orbit, or approximately every 3 h, during Earth occultation. One position of the instrument's filter wheel contains a set of ^{55}Fe radioactive sources providing a fiducial x-ray line at 5.9 keV. During Earth occultation, the filter wheel sources were rotated into the aperture, providing 30-min exposures with 500 counts in the 5.9-keV line per pixel per fiducial measurement. The fiducial measurements were then used to reconstruct the energy scale at that time step using the non-linear reconstruction method described in ref. 35. The energy scale was linearly interpolated between fiducial steps, which has been shown to be sufficient to reconstruct the energy scale to better than 0.3 eV at 5.9 keV (ref. 36), especially for the frequently sampled fiducials during this early observation. The summed, reconstructed fiducial measurements for the Cas A observations give a line shift error of <0.04 eV at 5.9 keV for the entire detector array. More detail can be found in appendix 1 of refs. 37.

Spectral Analysis

As shown in Fig. 1, we divided the field of view into three regions to investigate the spatial variation of odd-Z elements in the spectral analysis described below. For the SE region, we checked the spectrum of each pixel and selected pixels with a large equivalent width of K emissions (pixel IDs 17, 18, 25, 32, 33 and 34), where the distribution of the selected pixels is in good agreement with that of the O emissions. Each spectral fit was performed using SPEX software[38] version 3.08.01 and Xspec software[39] version 12.14.1 (AtomDB 3.1.0.v7) with the maximum-likelihood C statistic[40]: we analysed the Resolve spectrum in the 1.6–5.0-keV band, where any background component is negligible (but, of course, we considered the non-X-ray background emissions in our analysis, as described below). The spectral fit used in the main text is the result with Xspec. To evaluate the effect of the non-X-ray background (NXB), we use a temporal NXB spectral model provided by the XRISM calibration team. The NXB model was constructed from a stacked NXB event file based on night-Earth observations with a total exposure of 785 ks, and has a power law and 17 Gaussian lines for Al Kα1/Kα2, Au Mα1, Cr Kα1/Kα2, Mn Kα1/Kα2, Fe Kα1/Kα2, Ni Kα1/Kα2, Cu Kα1/Kα2, Au Lα1/Lα2 and Au Lβ1/Lβ2. In Fig. 2, the NXB contribution is taken into account in the modelling but is below the displayed range. The NXB model we used has no line features around the K He-like Kα emission. We have confirmed that the K/Ar ratios agree within the statistical error (only a few per cent change), whether or not the NXB model is considered.

On the basis of previous observations[25], the spectra were fitted with a two-component non-equilibrium ionization (NEI) model absorbed by the interstellar medium with the solar abundances[18]. For the ejecta component, we use a plane-parallel shock (pshock) plasma model (in the case of SPEX, 'Mode=3' in the neij model was used). The pshock and single NEI models give consistent results with respect to K detection, although the former gives a slightly better fit (Extended Data Table 1). We allowed the volume emission measure $\mathrm{VEM_{NEI}}$ ($=n_e n_p V_{\mathrm{NEI}}$, where n_e, n_p and V_{NEI} are the electron density, proton density and the volume of the plasma, respectively), the electron temperature kT_e and the ionization timescale $n_e t$ to vary. The abundances of Si, P, S, Cl, Ar, K and Ca were left free and tied between the two NEI components, while the others were fixed at the solar values. The absorption column density N_H was fixed at 1.9×10^{22} cm^{-2}, 2.0×10^{22} cm^{-2} and 1.5×10^{22} cm^{-2} for the SE, W and N region, respectively, based on previous observation[25]. Supplementary Fig. 1 shows the spectrum of the SE region along with the best-fit model consisting of two plasma components. These components, having different electron temperatures and line-of-sight velocities, both contribute to the observed line structures, complicating abundance measurements. For example, the N region exhibits a complex velocity structure, with redshifts varying across elements and ionization states[17], which makes it difficult to accurately determine the abundances of Cl and K, even though their

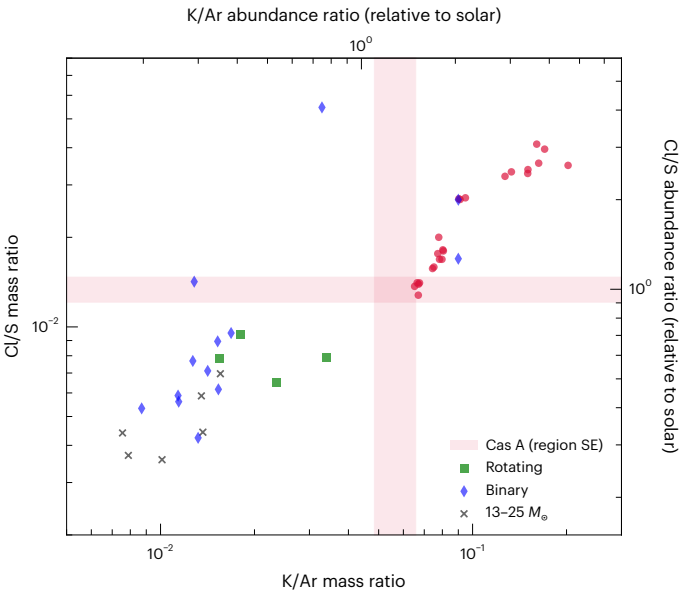

Fig. 4 | Observed Cl/S and K/Ar ratios in Cas A compared with representative nucleosynthesis models. The abundance ratio is defined as the elemental abundance ratio normalized to the solar value: $(\mathrm{K/Ar})/(\mathrm{K/Ar})_\odot$ and $(\mathrm{Cl/S})/(\mathrm{Cl/S})_\odot$. Red regions indicate the 1σ statistical confidence intervals of observed abundance ratios in the SE region. Model predictions are shown for non-rotating single-star progenitors with initial masses of 13–25$M_\odot$ from ref. 20 (grey crosses), rotating models from ref. 21 with initial masses of 13–25$M_\odot$ and rotational velocities of 300 km s^{-1} (green squares), shell merger candidates from a subset of the models in ref. 22 with progenitor masses of ~19–27$M_\odot$ (red circles) and binary star models from ref. 12 with initial masses of 13–25$M_\odot$ and companion stars with 80% of the primary mass (blue diamonds). All models shown assume solar metallicity. See Extended Data Fig. 2 for a more comprehensive comparison across a wider range of model parameters.

spectral features are clearly present. In contrast, the SE region shows a simpler velocity structure and narrower line widths compared with the N region (Fig. 2), allowing for more reliable abundance measurements. We confirmed that additional components such as non-thermal emission or another NEI model do not substantially affect the results for the SE region. On the other hand, in the N and W regions, if non-thermal emission is not considered, the temperature of the high-temperature plasma component exceeds 5 keV, which is higher than in other regions. Therefore, we added a power-law (non-thermal) component for the spectral fitting of the N and W regions. In these regions, previous studies have reported that non-thermal emission is strong[41–44], supporting the validity of adding the power-law component in this study. All the results are summarized in Table 2, showing that the two-component NEI model effectively explains all the Resolve spectra with statistically acceptable fits.

Several factors, such as differences in region selections, fit ranges and atomic codes, can introduce errors in abundance estimation. Here, we discuss systematic errors in abundance estimation (in particular, the K/Ar ratio, which is the focus of this study) by performing spectral analysis under various conditions. The XRISM calibration team does not recommend the asymmetric region selection used here because of the difficulty in evaluating contamination from other regions. For example, it is recommended to select a symmetrical region with a collection of 2 × 2 pixels. Therefore, we also analysed the 2 × 2 pixel region at the centre of the observation in the East region (pixel IDs 0, 17, 18 and 35), where the odd-Z elements seem to be concentrated. Even in this region, we found the K/Ar ratio to be 1.4 ± 0.2 with Xspec, which agrees with the result in region A. Here, the detection of K is 7.7σ. On the other hand, we emphasize that the effect of spatial–spectral mixing due to the point spread function of the telescope does not change our conclusion. In particular, in the eastern region used in the main text, the observed value of K/Ar ≈ 1 solar does not change even when using the Resolve full-array data. Also, whether we assume a single NEI plasma or a multi-temperature plasma, the result remains the same. Therefore, slight differences in region selection or plasma parameters do not change our conclusion. In a 2 × 2 pixel region, we can estimate with the raytracing code 'xrtraytrace' that ~50–60% of the radiation comes from within this region. Even though there is such a large amount of contamination from the neighbouring regions, it would be difficult to change the plasma parameters to overturn the conclusion.

In Extended Data Table 1, we summarize the K/Ar (also P/Si and Cl/S) ratios under different fitting conditions. It is found that the best-fit values agree within 10% in most cases. We checked the spectral fitting using a narrower energy band of 3.0–4.2 keV, which agrees well with the results in 1.6–5.0 keV. The electron loss continuum considered in the extra-large (XL) response matrix mainly affects the continuum component below 1.8 keV, so the large (L) matrix was used for the fitting in the 3.0-4.2-keV band without its effect. As mentioned in the main text, the emission lines of Ar and K can be explained by almost a single plasma model, thus we fitted the spectrum using a single NEI (pshock or nei) model in this energy band. The NXB model was not included in this analysis, because the NXB level is three orders of magnitude lower than the emissions from the remnant. In fitting over a wide energy band, the plasma parameters of K and Ar may be affected by other components and their abundance may change. On the other hand, even with this simple approach in the narrow band, the K/Ar ratios agree very well, supporting the robustness of our K/Ar measurements. In the case of Cl/S, the best-fit values agree within 40% in most cases, which implies larger systematic errors for the Cl observations. This is influenced by the difficulty in modelling the continuum emission; in particular, using a wider fitting energy range tends to result in a larger Cl/S ratio. A similar trend is also seen in the case of the P/Si ratio. These variations probably reflect the magnitude of systematic uncertainties, but even when taking them into account, our conclusions remain robust.

We also investigated a broader energy band from 1.6 to 12 keV, including the Fe K emissions. In this energy band, it is difficult to ignore the non-thermal emission even in the SE region, so a power-law component was added to the analysis (the NXB model is also included). Here, the photon index of the power-law component was fixed at a typical value of 2.3 (ref. 45), because it was difficult to determine. We confirmed that the mean values of the K/Ar ratios stay within the 1σ confidence range with any photon-index values in the range of 2.3–3.0 even in the cases of the W and N regions where the non-thermal components are more dominant than in the SE region. The addition of a power-law component can reduce the fitted continuum level of the thermal component, thereby resulting in higher abundance values as the line to continuum ratio increases. On the other hand, the K/Ar ratio is almost the same as those for the 1.6–5.0-keV band. The result with AtomDB has a slightly larger K/Ar ratio of 1.5, but the spectral fit around the Fe K band is worse than with SPEX. Currently, there is a discrepancy between atomic codes in the Fe band, and an update is planned. Since the uncertainty may affect the determination of the plasma parameters of K and Ar, the results in the 1.6–5-keV band are considered more reliable for the present analysis.

Supplementary Fig. 2 shows a comparison of the spectra in 3.0–4.2 keV generated by AtomDB and SPEX. In the energy band where the Ar and K emissions are present, there are some differences between the different atomic codes, but the spectral models are in good agreement. Several updates were made in these atomic databases to explain this observation of Cassiopeia A. In the case of AtomDB, the new data (version 3.1.0) include major improvements to the dielectronic recombination satellite lines for B-like to H-like ions; notably improved inner shell lines from excitation for the same, going up to n = 15; inclusion of the K-beta and K-gamma lines from inner shell excitation; and revised fluorescence yields for n = 3 and above inner shell lines. In the case of SPEX, a new calculation has been performed for Be- and Li-like Si, P, S, Cl Ar, and K, focusing on a complete set of inner-shell and dielectronic recombination transitions up to n = 7. For the dominant S He- and H-like transitions, SPEX now includes an extended calculation up to n = 52. The high Rydberg series of He-like S lines reproduce better the observed spectrum around 3.2 keV. Since the fits to the 3.2-keV feature may influence the measurement of the K abundance, a Gaussian component has been introduced into the model with AtomDB to compensate the atomic code difference. The two atomic codes currently agree on K/Ar with a difference of only a few per cent.

Model dependence on odd-Z yields

Nucleosynthetic studies have predicted that the fraction of odd-Z elements in SN ejecta depends on several stellar factors, for example, stellar rotation[21], binary interaction[12], internal activities[11] and initial metallicity[21]. To investigate these effects, we plot the final yields in ejecta in theoretical models with our observational results in Extended Data Fig. 1. The top panel shows the models provided by Limongi and Chieffi in ref. 21, in which they calculated the SN yield with different rotation velocities (v = 0, 150 and 300 km s^{-1}) and metallicities ([Fe/H] = −3, −2, −1 and 0). While the even-Z elements depend less on the parameters, the odd-Z element yields vary from the models with different parameters. In particular, K/Ar ratios appear to increase with both higher metallicities and faster rotational velocities. The middle panel shows the models of Farmer et al. from ref. 12, in which they surveyed effects of binary interactions by stellar simulations with the companions, whose initial masses were set to be 0.8 times the main stars. In the range of the plot, the K/Ar ratios are likely to be higher in the binary models, but the yields of other elements, including those with even Z, seem not to have clear dependence on whether the progenitor was a single star or a binary system. The bottom panel shows the models by Sukhbold et al.[22]. We analysed the mass fraction profiles at the onset of core collapse, and plot the yields of models in which the O-burning layers are merging with outer C-burning layers

(since this resembles the characteristics of a shell merger[29], hereafter we refer to this as a 'shell merger candidate') and those in which the distinct borders between the layers are maintained (see below; see Supplementary Fig. 3 and ref. 46 for more details). Consistent with ref. 11, the shell merger candidates show higher Cl and K yields than those of their models without shell merger.

To compare the relative contributions of these effects to the enhancement of odd-*Z* elements, we constructed a more comprehensive model plot of the K/Ar and Cl/S ratios, using the models of Nomoto et al.[20], Limongi and Chieffi[21] Roberti et al.[30], Farmer et al.[12] and Sukhbold et al.[22] (hereafter NKT13, LC18, R24, F23 and S16), incorporating our observational results (Extended Data Fig. 2). These models were computed using different stellar evolution codes (for example, KEPLER and FRANEC), each employing distinct nuclear reaction networks and treatments. However, as shown in Extended Data Fig. 2, the NKT13, LC18 and S16 models excepted for the shell merger candidates show similar ratios, implying that the variation due to code differences appears small compared with the range caused by physical parameters such as rotation, binarity and shell mergers. The K/Ar ratios and Cl/S ratios roughly show positive correlation, and those in shell merger candidates in the S16 and F23 models are probably able to enhance the odd-*Z* yields much more than rotating models. Both the K/Ar and Cl/S ratios in Cas A are close to the shell merger candidates in S16 models and both single and binary models of F23, rather than LC18 models incorporating stellar rotation and metallicity effects. R24 is an extension of LC18 to higher metallicity ([Fe/H] = 0.3, that is, twice solar). Although increased metallicity is known to enhance odd-*Z* element production, even the R24 models cannot reach the Cl/S and K/Ar ratios observed in Cas A. Given that the initial metallicity of Cas A is suggested to be sub-solar[47], the contribution of metallicity to the nucleosynthesis of odd-*Z* elements in Cas A is likely to be limited. While the S16 results may suggest that progenitors with initial masses of $\gtrsim 20 M_{\odot}$ tend to have enhanced odd-*Z* yields, it is important to note that the LC18 and NKT13 models in the similar mass range do not show such enhancements. This implies that the enhanced odd-*Z* element yields are unlikely to be a simple function of initial mass and instead highlight the importance of stellar processes such as shell mergers. We also note that, although binary progenitors have been suggested to enhance odd-*Z* yields, single-star models show variable values of these ratios, and even they can exhibit notably enhanced odd-*Z* yields.

While the enhancement of odd-*Z* elements such as K and Cl is often attributed to progenitor rotation or binary interaction, a closer inspection of our model survey reveals a more nuanced picture, indicating that additional mechanisms may be at play. To explore this point, we further investigated the mass fraction profiles of the models in Fig. 3; the results are shown in Supplementary Fig. 3. The top panel shows the $14.9 M_{\odot}$ model from Sukhbold et al. (S16), which retains a textbook, onion-like structure. In contrast, the bottom panel exhibits a structure where the Si-rich layer (O-burning layer) appears to be merging with the O/Ne-rich layer (C-burning layer). The mass fraction profiles of the binary and rotating progenitor models deviate from the canonical onion-skin structure, exhibiting signatures of partial mixing or merging between adjacent burning layers. It has been suggested that such layer merging is more likely to occur in rotating progenitor models[30], and some of the binary models used in this study have also been reported to exhibit similar structural features[48]. Furthermore, in ref. 12, Farmer et al. found that their models with abundant K produced the amount during their pre-SN phase and pointed out that the convective structure outside the Fe core is the key to the production. These results suggest that the internal structure at the final stage of stellar evolution may influence the yields of odd-*Z* elements as much as, or even more than, the initial stellar parameters. According to Ritter et al.[11], the pre-SN yields of odd-*Z* elements in such progenitors depend on the entrainment rate at the O/Si-burning shell. In other words, they are sensitive to the nature of the mixing processes occurring during the O/Si-burning phase shortly before or at the onset of core collapse. Furthermore, some multi-dimensional SN simulations suggest that such a convective state can result in asymmetry of the remnant[49]. Therefore, future deep observations of the asymmetric SNR Cas A, including spatially resolved abundance distributions, will provide further insight into the nucleosynthetic processes responsible for the excess production of odd-*Z* elements.

Data availability

The XRISM data are available via NASA at https://heasarc.gsfc.nasa.gov/docs/xrism/archive/.

Code availability

To analyse X-ray data with XRISM, we used public software, HEASoft (https://heasarc.gsfc.nasa.gov/docs/software/heasoft/). We used public atomic data in AtomDB (http://www.atomdb.org/) and SPEX (https://www.sron.nl/astrophysics-spex). We fitted the X-ray spectra with a public package, Xspec (https://heasarc.gsfc.nasa.gov/xanadu/xspec/).

References

1. Hughes, J. P., Rakowski, C. E., Burrows, D. N. & Slane, P. O. Nucleosynthesis and mixing in Cassiopeia A. *Astrophys. J. Lett.* **528**, 109–113 (2000).
2. Masseron, T. et al. Phosphorus-rich stars with unusual abundances are challenging theoretical predictions. *Nat. Commun.* **11**, 3759 (2020).
3. Xing, Q.-F. et al. A metal-poor star with abundances from a pair-instability supernova. *Nature* **618**, 712–715 (2023).
4. Koo, B.-C., Lee, Y.-H., Moon, D.-S., Yoon, S.-C. & Raymond, J. C. Phosphorus in the young supernova remnant Cassiopeia A. *Science* **342**, 1346–1348 (2013).
5. Bekki, K. & Tsujimoto, T. Phosphorus enrichment by one novae in the galaxy. *Astrophys. J. Lett.* **967**, 1 (2024).
6. Timmes, F. X., Woosley, S. E. & Weaver, T. A. Galactic chemical evolution: hydrogen through zinc. *Astrophys. J. Suppl. Ser.* **98**, 617 (1995).
7. Kobayashi, C., Umeda, H., Nomoto, K., Tominaga, N. & Ohkubo, T. Galactic chemical evolution: carbon through zinc. *Astrophys. J.* **653**, 1145–1171 (2006).
8. Kobayashi, C., Karakas, A. I. & Lugaro, M. The origin of elements from carbon to uranium. *Astrophys. J.* **900**, 179 (2020).
9. Prantzos, N., Abia, C., Limongi, M., Chieffi, A. & Cristallo, S. Chemical evolution with rotating massive star yields – I. The solar neighbourhood and the s-process elements. *Mon. Not. R. Astron. Soc.* **476**, 3432–3459 (2018).
10. Tominaga, N., Umeda, H. & Nomoto, K. Supernova nucleosynthesis in population III 13–50M_{solar} stars and abundance patterns of extremely metal-poor stars. *Astrophys. J.* **660**, 516–540 (2007).
11. Ritter, C. et al. Convective–reactive nucleosynthesis of K, Sc, Cl and p-process isotopes in O–C shell mergers. *Mon. Not. R. Astron. Soc.Letters* **474**, 1–6 (2018).
12. Farmer, R., Laplace, E., Ma, J.-z, de Mink, S. E. & Justham, S. Nucleosynthesis of binary-stripped stars. *Astrophys. J.* **948**, 111 (2023).
13. Gerardy, C. L. & Fesen, R. A. Near-infrared spectroscopy of the Cassiopeia A and Kepler supernova remnants. *Astrophys. J.* **121**, 2781 (2001).
14. Laming, J. M. & Temim, T. Element abundances in the unshocked ejecta of Cassiopeia A. *Astrophys. J.* **904**, 115 (2020).
15. Tashiro, M. et al. X-ray imaging and spectroscopy mission. *Publ. Astron. Soc. Jpn* **77**, S1–S9 (2025).
16. Wongwathanarat, A., Janka, H.-T., Müller, E., Pllumbi, E. & Wanajo, S. Production and distribution of ^{44}Ti and ^{56}Ni in a three-dimensional supernova model resembling Cassiopeia A. *Astrophys. J.* **842**, 13 (2017).

17. Suzuki, S. et al. Dynamics of the intermediate-mass-element ejecta in the supernova remnant Cassiopeia A studied with XRISM. *Publ. Astron. Soc. Jpn* **77**, S131–S143 (2025).
18. Lodders, K., Palme, H. & Gail, H.-P. Abundances of the elements in the Solar System. *Landolt-Börnstein* **4B**, 712 (2009).
19. Young, P. A. et al. Constraints on the progenitor of Cassiopeia A. *Astrophys. J.* **640**, 891 (2006).
20. Nomoto, K., Kobayashi, C. & Tominaga, N. Nucleosynthesis in stars and the chemical enrichment of galaxies. *Annu. Rev. Astron. Astrophys.* **51**, 457–509 (2013).
21. Limongi, M. & Chieffi, A. Presupernova evolution and explosive nucleosynthesis of rotating massive stars in the metallicity range $-3 \le [Fe/H] \le 0$. *Astrophys. J. Suppl. Ser.* **237**, 13 (2018).
22. Sukhbold, T., Ertl, T., Woosley, S., Brown, J. M. & Janka, H.-T. Core-collapse supernovae from 9 to 120 solar masses based on neutrino-powered explosions. *Astrophys. J.* **821**, 38 (2016).
23. Krause, O. et al. The Cassiopeia A supernova was of type IIb. *Science* **320**, 1195 (2008).
24. Vink, J., Kaastra, J. & Bleeker, J. A new mass estimate and puzzling abundances of snr cassiopeia a. *Astron. Astrophys.* **307**, 41–44 (1996).
25. Hwang, U. & Laming, J. M. A Chandra X-ray survey of ejecta in the Cassiopeia A supernova remnant. *Astrophys. J.* **746**, 130 (2012).
26. Sato, T. et al. Destratification in the progenitor interior of the Mg-rich supernova remnant N49B. *Astrophys. J.* **984**, 185 (2025).
27. Katsuda, S. et al. Discovery of X-ray-emitting O–Ne–Mg-rich ejecta in the galactic supernova remnant Puppis A. *Astrophys. J.* **714**, 1725–1732 (2010).
28. Bhalerao, J., Park, S., Schenck, A., Post, S. & Hughes, J. P. Detailed X-ray mapping of the shocked ejecta and circumstellar medium in the galactic core-collapse supernova remnant G292.0+1.8. *Astrophys. J.* **872**, 31 (2019).
29. Yadav, N., Müller, B., Janka, H. T., Melson, T. & Heger, A. Large-scale mixing in a violent oxygen–neon shell merger prior to a core-collapse supernova. *Astrophys. J.* **890**, 94 (2020).
30. Roberti, L., Limongi, M. & Chieffi, A. Zero and extremely low-metallicity rotating massive stars: evolution, explosion, and nucleosynthesis up to the heaviest nuclei. *Astrophys. J. Suppl. Ser.* **270**, 28 (2024).
31. Müller, B., Melson, T., Heger, A. & Janka, H.-T. Supernova simulations from a 3D progenitor model – Impact of perturbations and evolution of explosion properties. *Mon. Not. R. Astron. Soc.* **472**, 491–513 (2017).
32. Bollig, R. et al. Self-consistent 3D supernova models from −7 minutes to +7 s: a 1-bethe explosion of a 19$M_{\odot}$ progenitor. *Astrophys. J.* **915**, 28 (2021).
33. Bamba, A. et al. Measuring the asymmetric expansion of the Fe ejecta of Cassiopeia A with XRISM/Resolve. *Publ. Astron. Soc. Jpn* **77**, S144–S153 (2025).
34. Vink, J. et al. Mapping Cassiopeia A's silicon/sulfur Doppler velocities with XRISM/Resolve. *Publ. Astron. Soc. Jpn* **77**, S154–S170 (2025).
35. Porter, F. S. et al. Temporal gain correction for X-ray calorimeter spectrometers. *J. Low Temp. Phys.* **184**, 498–504 (2016).
36. Porter, F. S. et al. In-flight performance of the XRISM/Resolve detector system. In *Proc. Space Telescopes and Instrumentation 2024: Ultraviolet to Gamma Ray* (eds den Herder, J.-W.A., Nikzad, S. & Nakazawa, K.) https://doi.org/10.1117/12.3018882 (SPIE, 2024).
37. XRISM Collaboration. The XRISM first-light observation: velocity structure and thermal properties of the supernova remnant N 132D. *Publ. Astron. Soc. Jpn* **76**, 1186–1201 (2024).
38. Kaastra, J. S., Mewe, R. & Nieuwenhuijzen, H. SPEX: a new code for spectral analysis of X & UV spectra. In *UV and X-Ray Spectroscopy of Astrophysical and Laboratory Plasmas* (eds Yamashita, K. & Watanabe, T.) 411–414 (1996).
39. Arnaud, K. A. XSPEC: the first ten years. In *Astronomical Data Analysis Software and Systems V. ASP Conference Series* Vol. 101 (eds Jacoby, G. H. & Barnes, J.) 17–20 (Astronomical Society of the Pacific, 1996).
40. Cash, W. Parameter estimation in astronomy through application of the likelihood ratio. *Astrophys. J.* **228**, 939–947 (1979).
41. Helder, E. A. & Vink, J. Characterizing the nonthermal emission of Cassiopeia A. *Astrophys. J.* **686**, 1094–1102 (2008).
42. Uchiyama, Y. & Aharonian, F. A. Fast variability of nonthermal X-ray emission in Cassiopeia A: probing electron acceleration in reverse-shocked ejecta. *Astrophys. J. Lett.* **677**, 105 (2008).
43. Sato, T. et al. X-ray measurements of the particle acceleration properties at inward shocks in Cassiopeia A. *Astrophys. J.* **853**, 46 (2018).
44. Grefenstette, B. W. et al. Locating the most energetic electrons in Cassiopeia A. *Astrophys. J.* **802**, 15 (2015).
45. Patnaude, D. J. & Fesen, R. A. Proper motions and brightness variations of nonthermal X-ray filaments in the Cassiopeia A supernova remnant. *Astrophys. J.* **697**, 535–543 (2009).
46. Sato, T. et al. Inhomogeneous stellar mixing in the final hours before the Cassiopeia A supernova. *Astrophys. J.* **990**, 103 (2025).
47. Sato, T. et al. A subsolar metallicity progenitor for Cassiopeia A, the remnant of a type IIb supernova. *Astrophys. J.* **893**, 49 (2020).
48. Laplace, E. et al. Different to the core: the pre-supernova structures of massive single and binary-stripped stars. *Astron. Astrophys.* **656**, 58 (2021).
49. Couch, S. M. & Ott, C. D. Revival of the stalled core-collapse supernova shock triggered by precollapse asphericity in the progenitor star. *Astrophys. J. Lett.* **778**, 7 (2013).

Acknowledgements

This work was supported by JSPS KAKENHI grant nos. JP22H00158, JP22H01268, JP22K03624, JP23H04899, JP21K13963, JP24K00638, JP24K17105, JP21K13958, JP21H01095, JP23K20850, JP24H00253, JP21K03615, JP24K00677, JP20K14491, JP23H00151, JP19K21884, JP20H01947, JP20KK0071, JP23K20239, JP24K00672, JP24K17104, JP24K17093, JP20K04009, JP21H04493, JP20H01946, JP23K13154, JP23K13128, JP19K14762, JP20H05857, JP23K03459 and JP24KJ1485 and NASA grant nos. 80NSSC23K0650, 80NSSC20K0733, 80NSSC18K0978, 80NSSC20K0883, 80NSSC20K0737, 80NSSC24K0678, 80NSSC18K1684 and 80NNSC22K1922. L.C. acknowledges support from NSF award 2205918. C.D. acknowledges support from STFC through grant no. ST/T000244/1. L. Gu acknowledges financial support from Canadian Space Agency grant no. 18XARMSTMA. A.T. and the present research are in part supported by the Kagoshima University postdoctoral research programme (KU-DREAM). S. Yamada acknowledges support by the RIKEN SPDR Program. I.Z. acknowledges partial support from the Alfred P. Sloan Foundation through the Sloan Research Fellowship. M. Sawada acknowledges the support by the RIKEN Pioneering Project Evolution of Matter in the Universe (r-EMU) and Rikkyo University Special Fund for Research (Rikkyo SFR). Part of this work was performed under the auspices of the US Department of Energy by Lawrence Livermore National Laboratory under contract DE-AC52-07NA27344. The material is based upon work supported by NASA under award no. 80GSFC21M0002. This work was supported by the JSPS Core-to-Core Program, JPJSCCA20220002. The material is based on work supported by the Strategic Research Center of Saitama University.

Author contributions

T.S. led the Resolve data and pre-SN/SN model analysis and wrote the manuscript. K. Matsunaga analysed the nucleosynthesis models and the Resolve data and wrote the manuscript. H. Uchida is one of the authors who conceived this study, led the data analysis and prepared the manuscript. L. Gu performed a spatially resolved odd-*Z* search and

detailed spectral analysis of the remnant, and led the update of the SPEX database. A.F. updated the AtomDB database for explaining the observed spectra. M.A. analysed different combinations of Resolve pixels for the odd-*Z* element search. He confirmed that the detection of odd-*Z* elements is robust to small changes in pixel selection. J.V. and P.P. wrote the PV phase proposal for observing Cas A, which included the case for odd-*Z* detections using Resolve. P.P. also analysed the data and prepared the manuscript. F.S.P. reviewed the Resolve observations of the remnant as an instrumental expert and wrote the Resolve gain section. S. Katsuda helped to make the discussion about the low Ne/O ratio more robust. S.F. confirmed the abundance of odd-Z elements in a multi-dimensional SN model. H.Y., A.B., A. Simionescu, K.S., E.B. and R.M. helped to improve the manuscript. The science goals of XRISM were discussed and developed over 7 years by the XRISM Science Team, all members of which are authors of this manuscript. All the instruments were prepared by the joint efforts of the team. The manuscript was subject to an internal collaboration-wide review process. All authors reviewed and approved the final version of the manuscript.

Competing interests
The authors declare no competing interests.

Additional information
Extended data is available for this paper at https://doi.org/10.1038/s41550-025-02714-4.

Supplementary information The online version contains supplementary material available at https://doi.org/10.1038/s41550-025-02714-4.

Correspondence and requests for materials should be addressed to Toshiki Sato, Hiroyuki Uchida or Kai Matsunaga.

Peer review information *Nature Astronomy* thanks Bhagya Subrayan and the other, anonymous, reviewer(s) for their contribution to the peer review of this work.

Reprints and permissions information is available at www.nature.com/reprints.

Publisher's note Springer Nature remains neutral with regard to jurisdictional claims in published maps and institutional affiliations.

Open Access This article is licensed under a Creative Commons Attribution-NonCommercial-NoDerivatives 4.0 International License, which permits any non-commercial use, sharing, distribution and reproduction in any medium or format, as long as you give appropriate credit to the original author(s) and the source, provide a link to the Creative Commons licence, and indicate if you modified the licensed material. You do not have permission under this licence to share adapted material derived from this article or parts of it. The images or other third party material in this article are included in the article's Creative Commons licence, unless indicated otherwise in a credit line to the material. If material is not included in the article's Creative Commons licence and your intended use is not permitted by statutory regulation or exceeds the permitted use, you will need to obtain permission directly from the copyright holder. To view a copy of this licence, visit http://creativecommons.org/licenses/by-nc-nd/4.0/.

© The Author(s) 2025

XRISM collaboration

Marc Audard[1], Hisamitsu Awaki[2], Ralf Ballhausen[3,4,5], Aya Bamba[6], Ehud Behar[7], Rozenn Boissay-Malaquin[4,8], Laura Brenneman[9], Gregory V. Brown[10], Lia Corrales[11], Elisa Costantini[12], Renata Cumbee[4], Maria Diaz-Trigo[13], Chris Done[14], Tadayasu Dotani[15], Ken Ebisawa[15], Megan Eckart[10], Dominique Eckert[1], Teruaki Enoto[16], Satoshi Eguchi[17], Yuichiro Ezoe[18], Adam Foster[9], Ryuichi Fujimoto[15], Yutaka Fujita[18], Yasushi Fukazawa[19], Kotaro Fukushima[15], Akihiro Furuzawa[20], Luigi Gallo[21], Javier A. Garcia[4,22], Liyi Gu[12], Matteo Guainazzi[23], Kouichi Hagino[6], Kenji Hamaguchi[4,5,8], Isamu Hatsukade[24], Katsuhiro Hayashi[15], Takayuki Hayashi[4,5,8], Natalie Hell[10], Edmund Hodges-Kluck[4], Ann Hornschemeier[4], Yuto Ichinohe[25], Daiki Ishi[15], Manabu Ishida[15], Kumi Ishikawa[18], Yoshitaka Ishisaki[18], Jelle Kaastra[12,26], Timothy Kallman[4], Erin Kara[27], Satoru Katsuda[28], Yoshiaki Kanemaru[15], Richard Kelley[4], Caroline Kilbourne[4], Shunji Kitamoto[29], Shogo Kobayashi[30], Takayoshi Kohmura[31], Aya Kubota[32], Maurice Leutenegger[4], Michael Loewenstein[3,4,5], Yoshitomo Maeda[15], Maxim Markevitch[4], Hironori Matsumoto[33], Kyoko Matsushita[30], Dan McCammon[34], Brian McNamara[35], François Mernier[3,4,5], Eric D. Miller[27], Jon M. Miller[11], Ikuyuki Mitsuishi[36], Misaki Mizumoto[37], Tsunefumi Mizuno[38], Koji Mori[24], Koji Mukai[4,5,8], Hiroshi Murakami[39], Richard Mushotzky[3], Hiroshi Nakajima[40], Kazuhiro Nakazawa[36], Jan-Uwe Ness[41], Kumiko Nobukawa[42], Masayoshi Nobukawa[43], Hirofumi Noda[44], Hirokazu Odaka[33], Shoji Ogawa[15], Anna Ogorzalek[3,4,5], Takashi Okajima[4], Naomi Ota[45], Stephane Paltani[1], Robert Petre[4], Paul Plucinsky[9], Frederick Scott Porter[4], Katja Pottschmidt[4,5,8], Kosuke Sato[28,46], Toshiki Sato[47] ✉, Makoto Sawada[29], Hiromi Seta[18], Megumi Shidatsu[2], Aurora Simionescu[12], Randall Smith[9], Hiromasa Suzuki[15], Andrew Szymkowiak[48], Hiromitsu Takahashi[19], Mai Takeo[28], Toru Tamagawa[25], Keisuke Tamura[4,5,8], Takaaki Tanaka[49], Atsushi Tanimoto[50], Makoto Tashiro[15,28], Yukikatsu Terada[15,28], Yuichi Terashima[2], Yohko Tsuboi[51], Masahiro Tsujimoto[15], Hiroshi Tsunemi[33], Takeshi G. Tsuru[16], Hiroyuki Uchida[16] ✉, Nagomi Uchida[15], Yuusuke Uchida[31], Hideki Uchiyama[52], Yoshihiro Ueda[53], Shinichiro Uno[54], Jacco Vink[55], Shin Watanabe[15], Brian J. Williams[4], Satoshi Yamada[56], Shinya Yamada[29], Hiroya Yamaguchi[15], Kazutaka Yamaoka[36], Noriko Yamasaki[15], Makoto Yamauchi[24], Shigeo Yamauchi[45], Tahir Yaqoob[4,5,8], Tomokage Yoneyama[51], Tessei Yoshida[15], Mihoko Yukita[4,57], Irina Zhuravleva[58], Shin-ichiro Fujimoto[59], Kai Matsunaga[16] ✉ & Manan Agarwal[55]

[1]Department of Astronomy, University of Geneva, Versoix, Switzerland. [2]Department of Physics, Ehime University, Ehime, Japan. [3]Department of Astronomy, University of Maryland, College Park, MD, USA. [4]NASA/Goddard Space Flight Center, Greenbelt, MD, USA. [5]Center for Research and Exploration in Space Science and Technology, NASA/GSFC, Greenbelt, MD, USA. [6]Department of Physics, University of Tokyo, Tokyo, Japan. [7]Department of Physics, Technion, Technion City, Haifa, Israel. [8]Center for Space Science and Technology, University of Maryland Baltimore County, Baltimore, MD,

USA. [9]Center for Astrophysics, Harvard-Smithsonian, Cambridge, MA, USA. [10]Lawrence Livermore National Laboratory, Livermore, CA, USA. [11]Department of Astronomy, University of Michigan, Ann Arbor, MI, USA. [12]SRON Netherlands Institute for Space Research, Leiden, The Netherlands. [13]ESO, Garching bei München, Germany. [14]Centre for Extragalactic Astronomy, Department of Physics, University of Durham, Durham, UK. [15]Institute of Space and Astronautical Science, Japan Aerospace Exploration Agency, Kanagawa, Japan. [16]Department of Physics, Kyoto University, Kyoto, Japan. [17]Department of Economics, Kumamoto Gakuen University, Kumamoto, Japan. [18]Department of Physics, Tokyo Metropolitan University, Tokyo, Japan. [19]Department of Physics, Hiroshima University, Hiroshima, Japan. [20]Department of Physics, Fujita Health University, Aichi, Japan. [21]Department of Astronomy and Physics, Saint Mary's University, Halifax, Nova Scotia, Canada. [22]Cahill Center for Astronomy and Astrophysics, California Institute of Technology, Pasadena, CA, USA. [23]European Space Research and Technology Centre, European Space Agency, Noordwijk, The Netherlands. [24]Faculty of Engineering, University of Miyazaki, Miyazaki, Japan. [25]RIKEN Nishina Center, Saitama, Japan. [26]Leiden Observatory, University of Leiden, Leiden, The Netherlands. [27]Kavli Institute for Astrophysics and Space Research, Massachusetts Institute of Technology, Cambridge, MA, USA. [28]Department of Physics, Saitama University, Saitama, Japan. [29]Department of Physics, Rikkyo University, Tokyo, Japan. [30]Faculty of Physics, Tokyo University of Science, Tokyo, Japan. [31]Faculty of Science and Technology, Tokyo University of Science, Chiba, Japan. [32]Department of Electronic Information Systems, Shibaura Institute of Technology, Saitama, Japan. [33]Department of Earth and Space Science, Osaka University, Osaka, Japan. [34]Department of Physics, University of Wisconsin, Madison, WI, USA. [35]Department of Physics and Astronomy, University of Waterloo, Waterloo, Ontario, Canada. [36]Department of Physics, Nagoya University, Aichi, Japan. [37]Science Research Education Unit, University of Teacher Education Fukuoka, Fukuoka, Japan. [38]Hiroshima Astrophysical Science Center, Hiroshima University, Hiroshima, Japan. [39]Department of Data Science, Tohoku Gakuin University, Miyagi, Japan. [40]College of Science and Engineering, Kanto Gakuin University, Kanagawa, Japan. [41]European Space Astronomy Centre, European Space Agency, Madrid, Spain. [42]Department of Science, Faculty of Science and Engineering, KINDAI University, Osaka, Japan. [43]Department of Teacher Training and School Education, Nara University of Education, Nara, Japan. [44]Astronomical Institute, Tohoku University, Miyagi, Japan. [45]Department of Physics, Nara Women's University, Nara, Japan. [46]International Center for Quantum-Field Measurement Systems for Studies of the Universe and Particles, High Energy Accelerator Research Organization, Tsukuba, Japan. [47]School of Science and Technology, Meiji University, Kanagawa, Japan. [48]Yale Center for Astronomy and Astrophysics, Yale University, New Haven, CT, USA. [49]Department of Physics, Konan University, Hyogo, Japan. [50]Graduate School of Science and Engineering, Kagoshima University, Kagoshima, Japan. [51]Department of Physics, Chuo University, Tokyo, Japan. [52]Faculty of Education, Shizuoka University, Shizuoka, Japan. [53]Department of Astronomy, Kyoto University, Kyoto, Japan. [54]Nihon Fukushi University, Shizuoka, Japan. [55]Anton Pannekoek Institute, University of Amsterdam, Amsterdam, The Netherlands. [56]Frontier Research Institute for Interdisciplinary Sciences, Tohoku University, Sendai, Japan. [57]Johns Hopkins University, Baltimore, MD, USA. [58]Department of Astronomy and Astrophysics, University of Chicago, Chicago, IL, USA. [59]Department of Control and Information Systems Engineering, National Institute of Technology, Kumamoto College, Kumamoto, Japan. ✉e-mail: toshiki@meiji.ac.jp; uchida@cr.scphys.kyoto-u.ac.jp; matsunaga.kai.i47@kyoto-u.jp

https://doi.org/10.1038/s41550-025-02714-4

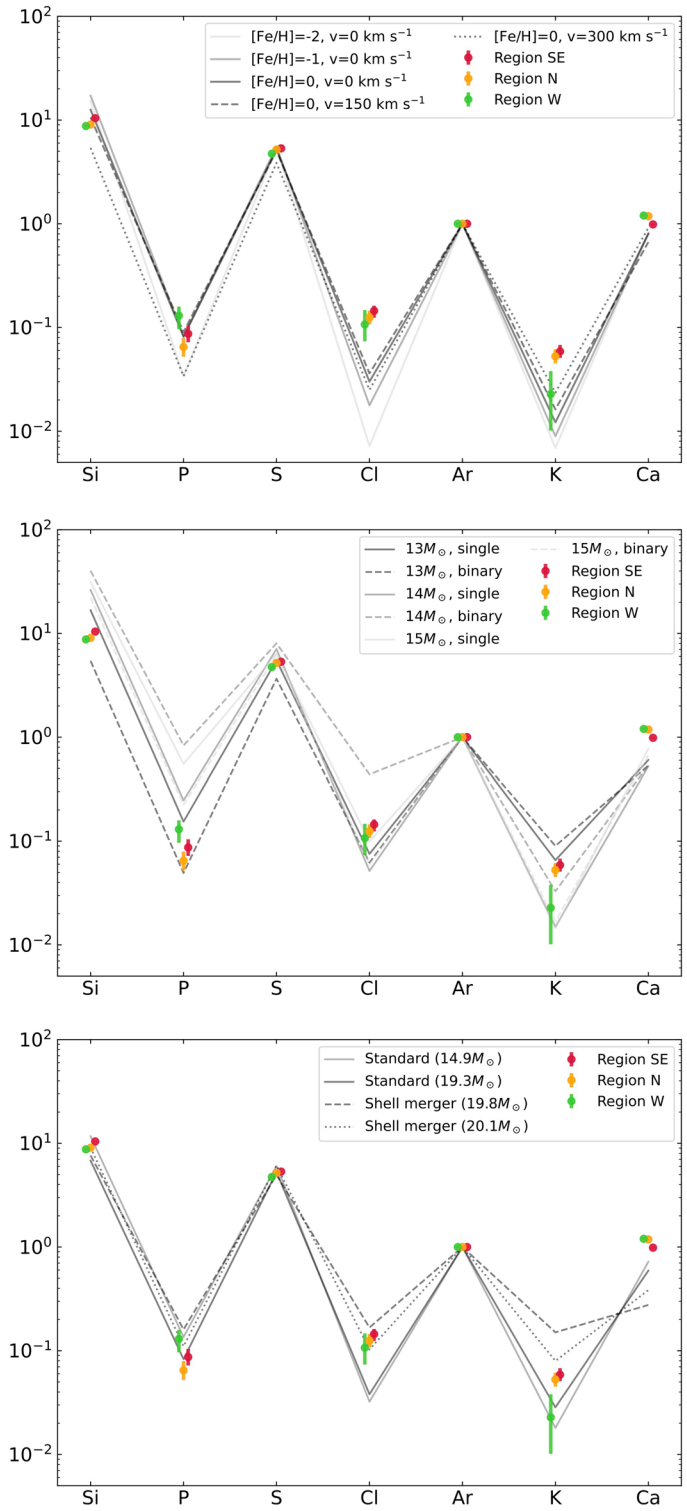

Extended Data Fig. 1 | Elemental mass ratios in Cas A compared to supernova nucleosynthesis models across a wider range of model parameters. Top: Comparison with 15$M_\odot$ models with the several initial metalicities ([Fe/H]= − 2, − 1, 0) and rotation velocities (v = 0, 150, 300 km s^{-1}) provided by Limongi & Chieffi[21]. Middle: Comparison with 13, 14, 15, 16$M_\odot$ models of the single star cases and the binary cases provided by farmer et al.[12]. In each binary case, the companion star mass is set to 0.8 times of the progenitor. Bottom: Comparison with non-rotating single star models with several masses provided by Sukhbold et al.[22]. The 14.9$M_\odot$ and 19.3$M_\odot$ models shows onion-like layers constituted with O-, Ne-, and C-burning layers. In contrast, in the 19.8$M_\odot$ and 20.1$M_\odot$ models, the O-burning layers are merging with the outer layers like shell mergers (see Figure ?). To facilitate comparison between the observed values and the model values, only the model values are connected with lines.

https://doi.org/10.1038/s41550-025-02714-4

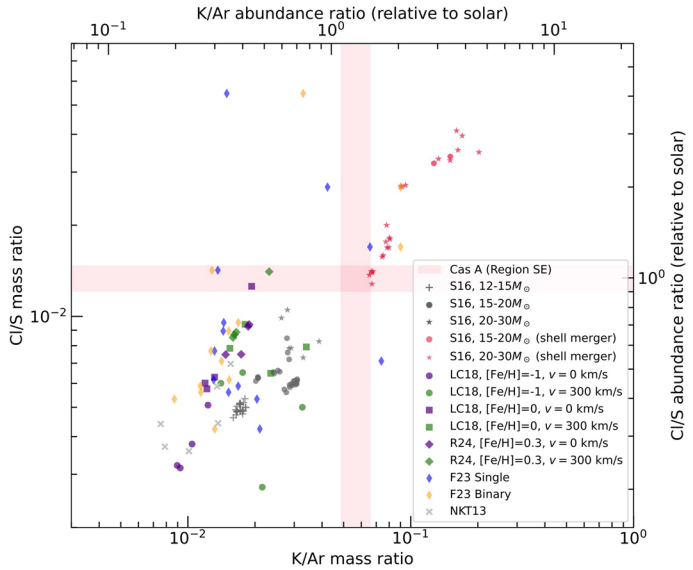

Extended Data Fig. 2 | Comparison between observed and predicted Cl/S and K/Ar ratios across multiple stellar models. The hatched light blue regions represent the 1σ confidence intervals for the observed mass ratios in region SE of Cas A. Sukhbold et al.[22] models (12-30 $M_\odot$) are shown with different marker shapes for progenitor mass ranges (circle: 12-15 $M_\odot$, square: 15-20 $M_\odot$, star: 20-30 $M_\odot$). Shell merger candidates are highlighted in red; non-merger models are shown in black. Models from Limongi & Chieffi[21] (13-25 $M_\odot$) are shown with squares and circles representing solar and sub-solar metallicity ([Fe/H] = −1 and 0), respectively. Rotation is indicated by color: purple for non-rotating and green for rotating models at 300 km s^{-1}. Roberti et al.[30] models extend LC18 to super-solar metallicity ([Fe/H] = 0.3), and are plotted in a similar format (non-rotating and rotating cases). Farmer et al.[12] models (10-30 $M_\odot$) are shown as stars: blue for single-star models and orange for binary models. Nomoto et al.[20] models (10-30 $M_\odot$) are indicated as grey crosses. The figure shows that models involving shell mergers or binary interactions can produce enhanced Cl and K abundances, consistent with our observational constraints.

https://doi.org/10.1038/s41550-025-02714-4

Extended Data Table 1 | Abundunce ratios obtained from different fitting conditions

Fitting range	Atomic Database	RMF matrix	P/Si	Cl/S	K/Ar	C-value/d.o.f
Region SE						
1.6–5.0 keV	AtomDB	XL	0.9±0.2	1.0±0.1	1.3±0.2	1.10
1.6–5.0 keV	SPEX	XL	0.9±0.2	$0.7^{+0.2}_{-0.1}$	1.2±0.2	1.29
3.0–4.2 keV	AtomDB (pshock)	L	—	—	1.3±0.2	1.05
3.0–4.2 keV	AtomDB (NEI)	L	—	—	1.2±0.2	1.08
3.0–4.2 keV	SPEX	L	—	—	1.2±0.2	1.15
1.6–12.0 keV	AtomDB	XL	1.5±0.2	1.4±0.2	1.5±0.2	0.95
1.6–12.0 keV	SPEX	XL	1.2±0.2	1.1±0.2	1.4±0.2	1.24
Region W						
1.6–5.0 keV	AtomDB	XL	1.7±0.4	0.9±0.3	0.5±0.3	1.04
1.6–15.0 keV	AtomDB	XL	1.9±0.4	1.2±0.3	0.8±0.3	0.89
Region N						
1.6–5.0 keV	AtomDB	XL	0.8±0.2	0.9±0.1	1.1±0.2	1.06
1.6–15.0 keV	AtomDB	XL	0.8±0.3	1.1±0.2	1.4±0.2	0.84

Note. The elemental ratios show elemental abundance ratios relative to the solar values, such as $(X/Y)/(X/Y)_{\odot}$.